Journal of Power Sources 202 (2012) 200–208

Contents lists available at SciVerse ScienceDirect

Journal of Power Sources

journal homepage: www.elsevier.com/locate/jpowsour

Carbon nanotube-supported Pt-Co bimetallic catalysts for preferential oxidation of CO in a H_2-rich stream with CO_2 and H_2O vapor

Chao Wang, Bodong Li, Haiqiang Lin, Youzhu Yuan*

State Key Laboratory of Physical Chemistry of Solid Surfaces, National Engineering Laboratory for Green Chemical Productions of Alcohol–Ethers–Esters, College of Chemistry and Chemical Engineering, Xiamen University, Xiamen 361005, PR China

ARTICLE INFO

Article history:
Received 12 August 2011
Received in revised form 7 November 2011
Accepted 15 November 2011
Available online 25 November 2011

Keywords:
Hydrogen purification
CO preferential oxidation
Platinum
Cobalt
Carbon nanotube

ABSTRACT

Carbon nanotube-supported Pt-Co bimetallic catalysts (Pt-Co/CNTs) are prepared for preferential oxidation of CO in a H_2-rich stream. The results indicate that the addition of Co into the Pt/CNT catalyst significantly improves catalytic performance, making it superior to other carriers supporting the same composition of Pt–Co. Optimized bimetallic Pt-Co/CNT catalyst can preferentially oxidize dilute CO in a H_2-rich stream at a wide temperature window of 313–433 K. At a temperature of 353 K and a H_2-rich stream with 1% CO, 0.7–0.8% O_2, 20% H_2O, 25% CO_2 and 50% H_2 balanced with N_2, this catalyst can afford 100% CO conversion with 62–71% O_2 selectivity for over 100 h. The transmission electron microscopic images reveal that the metal nanoparticles are uniformly dispersed on the surfaces of CNTs with an average size of approximately 2–3 nm, independent of Co loading. The results of X-ray photoelectron spectroscopy and nanoscale elemental mapping indicate that most of Co species are in the form of CoO, presenting on the Pt domain. Higher performance of the Pt-Co/CNT is attributed to the interactions between the Pt nanoparticles and CoO, those are supported on CNT surfaces.

1. Introduction

Proton exchange membrane fuel cells (PEMFCs) with H_2-rich gases as fuel are known as clean energy systems with a high thermodynamic efficiency [1]. However, the serious poisoning of Pt-anode by a trace of CO in H_2 is potentially a serious problem [2,3]. Currently, hydrogen may be purified by preferential oxidation of CO (CO-PROX) to decrease CO concentration less than 10 ppm at 423 K and then supplied to the PEMFCs at 353 K [4]. Thus, if the PROX can be performed below 353 K, the number of cooling processes will be reduced in the practical production of H_2. Moreover, the cold-start in PEMFCs is also a challenging research for automotive application [5,6] which requires the high quality purified hydrogen supply at room temperature as a fuel.

Although considerable progresses have been made towards the developments of active and selective Ru catalysts [7–9], the melioration of the CO-PROX activity at low temperature and avoidance of CO methanation at high temperature still need further improvement. In recent years, other supported noble metal catalysts, such as Pt, Pd, Au, and Rh, have also been employed for the CO-PROX reaction in a H_2-rich gas [10–15]. Among them, the catalysts formulated with Pt and Au have been extensively investigated. It is well known that Au catalysts are more active at lower temperatures but they inevitably show deactivation, whereas the Pt catalysts usually perform noticeable activities only under practical conditions above 423 K because of strong absorption between the CO species and Pt surface [16]. To solve this problem, different promoters, such as cobalt, iron, nickel, copper, rare earth oxides, and alkali metals, have been investigated for the purpose of improving the low temperature CO-PROX performance of the catalysts [17–25].

Generally, the reformate H_2-rich stream through a water-gas shift reaction contains 15–25% CO_2 and approximately 10–20% H_2O vapor. Landon et al. reported that Au/Fe_2O_3 catalysts are highly active for CO oxidation at 353 K; however, O_2 selectivity is as low as 51% in the presence of H_2O and CO_2 [26]. Avgouropoulos et al. found that negative effects of CO_2 and H_2O on the performance of no precious metal catalyst of CuO/CeO_2 and that temperature higher than 423 K is required for sufficient CO conversion (>90%) [27]. Therefore, developing a catalyst with high CO-PROX activity and tolerance to the presence of CO_2 and H_2O remains among the primary research interests in this field.

The monometallic Pt catalyst supported on multiwall carbon nanotubes (Pt/CNTs) with Pt loading as high as 15 wt% was shown to be very active for CO-PROX reaction at room temperature in a reaction mixture of 2.5 vol% CO, 2.5 vol% O_2, 25 vol% H_2, and N_2 balance [28]. There were promotional effects of Ni–MgO and $Fe–Al_2O_3$ dopants on the CO-PROX of Pt catalysts supported on CNTs, carbon nanofiber, graphite, and amorphous carbon [29–31]. However, the tolerance to CO_2 and H_2O needs further improvement. In addition, the amount of precious Pt to prepare CO-PROX

* Corresponding author. Tel.: +86 592 2181659; fax: +86 592 2183047.
E-mail address: yzyuan@xmu.edu.cn (Y. Yuan).

0378-7753/$ – see front matter © 2011 Elsevier B.V. All rights reserved.
doi:10.1016/j.jpowsour.2011.11.044

catalysts should be reduced without sacrificing performance at lower temperatures.

Herein, we report that a method of liquid-phase reduction using formaldehyde followed by calcination in air can prepare a Pt-Co/CNT bimetallic catalyst promising for CO-PROX with CO_2 and H_2O vapor at lower temperatures. The detailed structural and kinetic studies that address the effects of Co are also herein presented.

2. Experimental

2.1. Catalyst preparation

Carbon nanotubes (CNTs) were prepared by flowing CH_4 over a Ni-MgO catalyst in a fixed-bed reactor [32]. The obtained CNTs have multiwall fishbone-type structures with an outer diameter of 10–60 nm and an inner diameter of 2–4 nm. The Al_2O_3, SiO_2, and graphite (GA) were purchased from Sinopharm Chemical Reagent Co., Ltd. The active carbon (AC) was purchased from Guangxi Yebao Active Carbon Co., Ltd., and the TiO_2 (P-25) was obtained from Degussa AG Co., Ltd. Prior to use, the AC was pretreated in concentrated HNO_3 (68 wt%) at 363 K for 4 h under reflux conditions to remove amorphous carbon. Meanwhile, Al_2O_3 was calcined in air at 873 K for 4 h. The as-received CNTs were pretreated in concentrated HNO_3 (68 wt%) at 353 K under refluxing conditions to remove amorphous carbon and the remaining Ni-MgO catalyst. The purified CNTs were then filtered and washed with distilled water until the pH value reached 7, then dried under a vacuum overnight at 383 K.

The bimetallic Pt-Co catalysts were prepared from H_2PtCl_6 and $Co(NO_3)_2$. The supports were dispersed in aqueous solutions of H_2PtCl_6 and $Co(NO_3)_2$. After evaporation, the solids were added into aqueous solution of formaldehyde. The suspension was refluxed at 363 K for 30 min. The solids were collected by filtration; then they were dried overnight at 383 K and calcined in the air at 623 K for 4 h, affording the final catalysts. The metal loadings of Pt and Co was preset at 4 and 0–2 wt%, respectively. For comparison, 4.0% Pt/CNT, 5.0% Co/CNT, and Pt-Co catalysts supported on different carriers were also prepared using the same procedures.

2.2. Catalyst characterization

Powder X-ray diffraction (XRD) patterns were taken on a Phillips Panalytical X′pert Pro diffractometer and equipped with a graphite monochrometer and Cu-K_α radiation source (40 kV and 30 mA). Transmission electron microscopy (TEM) images were taken using a Tecnai F30 electron microscope operated at an acceleration voltage of 300 kV. The powder was dispersed in ethanol by ultrasonication for at least 30 min. Drops of suspensions were deposited on a copper grid coated with carbon. The statistical mean diameter of the nanoparticles was measured by counting at least 300 particles for each catalyst.

X-ray photoelectron spectroscopy (XPS) was performed using a Thermo Scientific Multilab 2000 instrument. The samples were cooled down to room temperature after treatment and sealed immediately under Ar and then they were transferred to a UHV chamber to avoid contacting with air as much as possible. The spectra were recorded at room temperature and the binding energy (BE) was referred to 284.6 eV for C 1s. Peak deconvolution and fitting were performed using the peak-fitting software with the spin-orbit splitting and the relative intensities of the spin-orbit components fixed.

Nitrogen adsorption–desorption isotherm was measured at 77 K on a Micromeritics TriStar 3020 sorptometer. The sample was outgassed at 573 K for 3 h before each measurement. The specific surface area was calculated following the Brunauer–Emmett–Teller (BET) method. The average pore diameter and total pore volume were determined by the Barret–Joyner–Halenda (BJH) method, according to the desorption isotherm branch.

The metal dispersions at different states were determined by O_2–H_2 titration on a Mircometrics ASAP 2020 instrument. The as-calcined sample (100 mg), after being evacuated at 313 K for 30 min, was first titrated with O_2 (99.999%) at 313 K. Subsequently, the sample was reduced with 5% H_2–95% Ar at 523 K for 30 min and then it was evacuated at the temperature for 30 min to remove the adsorbed hydrogen species. After being cooled down to 313 K under vacuum and evacuated at 313 K for another 30 min, the sample was titrated with O_2 at 313 K to give a metal dispersion by assuming O/Pt = 1 stoichiometry. Theoretically, the reduction process may leave the H species chemisorbed on the Pt surface and the O_2 molecule reacts first with the Pt–H and then the surface metallic Pt. The stoichiometry is accepted to be O/Pt = 1.5. However, in the actual O_2 titration process, the dispersion of monometallic Pt catalyst calculated from the O_2 adsorption volume by setting O/Pt = 1.5 stoichiometry was much smaller than that estimated from the TEM average particle size by using the equation $D = 1.13/d$ (where D is the Pt dispersion and d is the Pt particle diameter determined by TEM) [33,34]. Therefore, we used the stoichiometric $O/Pt_{surf} = 1$ by assuming the H species adsorbed on the surface of metallic Pt has been swept by evacuation. Further, the O_2 saturated sample was soaked in a 110 kPa of reaction feed gas (1% CO, 1% O_2, and 50% H_2 balanced with N_2) at a given temperature (313 K or 353 K) three times (3×10 min) and then evacuated at the given temperature for 30 min. After that, the sample was titrated with O_2 at the temperature to give a metal dispersion by assuming O/Pt = 1 stoichiometry. After the sample was titrated by oxygen at 313 K followed by evacuation at 313 K for 30 min to purge out any residual oxygen, H_2 titration was performed at this temperature to reconfirm the dispersion of Pt by using stoichiometry H/Pt = 3 due to the following reactions:

$$Pt_s + 1/2O_2 \rightarrow Pt_s\text{–}O \quad (1)$$

$$Pt_s\text{–}O + 3/2H_2 \rightarrow Pt_s\text{–}H + H_2O \quad (2)$$

Raman spectra were recorded at ambient temperature on a Renishaw inVia Raman microscope with an argon-ion laser at an excitation wavelength of 514 nm. The intensity of laser source was adjusted to 10%, and the final sample spectra were obtained by superposition of three measurement results to minimize the fluctuation of the spectra and improve the signal-to-noise ratio.

The Co and Pt loadings of the samples were determined by inductively coupled plasma atomic emission spectrometer (ICP-AES) using a Thermo Elemental IRIS Intrepid II XSP. The sample was treated by aqua regia at 363 K for 30 min, and the resultant solution was heated until it evaporated. The residue was diluted with 5% HCl and filtrated to a 25 mL volumetric flask before ICP-AES measurement.

2.3. Catalytic testing

The catalytic performances were examined in a conventional fixed-bed flow reactor using 100 mg of catalyst at 0.1 MPa, as previously reported [35]. The reactant mixture was adjusted by mass flow controllers with compositions of $CO/O_2/H_2/N_2 = 1/1/50/48$ (mol%) for PROX reaction and $CO/O_2/N_2 = 1/1/98$ for CO oxidation reaction. The ratio of total gaseous reactant flow rate to catalyst weight (FW^{-1}) was 30,000 mL h^{-1} g^{-1}. The mixed gas was passed through a tube containing NaOH pellets for purification. The effects of CO_2 and H_2O coexistence in the feed gas were observed at the reactant mixture of 1% CO, 0.5–1.0% O_2, 50% H_2, 25% CO_2, and 20% H_2O balanced with N_2, and the FW^{-1} adjusted to 40,000 mL g^{-1} h^{-1}.

Table 1
Physicochemical properties of CNT-supported Pt-Co bimetallic catalysts.[a]

Sample	Pt content (wt%)[a]	Co content (wt%)[a]	S_{BET} ($m^2\ g^{-1}$)	Average pore diameter (nm)
4.0% Pt/CNT	3.71	<0.01	119.6	3.2
4.0% Pt-0.3% Co/CNT	3.64	0.31	130.2	3.1
4.0% Pt-0.7% Co/CNT	3.43	0.60	137.7	3.1
4.0% Pt-1.3% Co/CNT	3.82	1.14	143.6	3.2
4.0% Pt-2.0% Co/CNT	3.57	1.78	148.5	3.0

[a] Determined by ICP-AES.

The outlet stream was analyzed by an online gas chromatograph. The CO conversion and O_2 selectivity were calculated by three equations, as reported elsewhere [35]. The turnover frequency (TOF) was calculated by evaluating the surface area of exposed Pt atoms in the reduced sample from the chemical adsorption of oxygen at 313 K.

3. Results and discussion

3.1. Catalyst characterization

3.1.1. Measurements of ICP-AES and N_2 physisorption

Surface oxygen-containing groups on a carbonaceous support, including carboxylic, carbonyl, and hydroxyl moieties, are generally considered initially indispensable in enhancing the hydrophilicity of the CNTs in aqueous solution [36]. In addition, these groups can serve as specific anchoring sites for the deposition of Pt and Co species, thereby facilitating their high dispersions on the surfaces of CNTs [37]. However, calcination after the conventional hydrogen reduction may lead to an aggregation of Pt nanoparticles, even if they are anchored on the surface of CNTs through the functional groups during reduction. Therefore, we adopted the liquid phase reduction method to reinforce the dispersion of active metals.

We prepared a series of supported Pt-Co bimetallic catalysts with fixed Pt loading at *ca.* 4.0 wt% and varying Co loadings at nominal 0–2.0 wt%. The contents of Co and Pt were measured by ICP-AES. The results are listed in Table 1, which shows that the Pt content in all the samples are quite similar and the actual Co content is close to the theoretical value. The textural characters of the catalysts are also summarized in Table 1. The loading of Co on the CNTs leads to an obvious increase of the surface area, which may be attributed to the activation and etching effects by the Co species. The phenomenon becomes more evident as the Co loading amount is increased. However, the average pore diameters show insignificant changes among the prepared catalysts, indicating that the deposition of Pt-Co merely introduces the defects on the surfaces of CNTs but without causing collapse of the tube structure of CNTs.

3.1.2. Raman measurement

The defect densities in CNTs were checked by Raman spectroscopy, as shown in Fig. 1. The peak at approximately 1342 cm^{-1} is assigned to the disordered graphite structure (D-band), and the high frequency peak at approximately 1576 cm^{-1} corresponds to a splitting of the E_{2g} stretching mode of graphite (G-band). The latter reflects the structural intensity of the sp^2-hybridized carbon atoms [38]. The higher intensity ratio of D-band to G-band (I_D/I_G) suggests the higher extent of defects in CNTs [39]. Here, I_D/I_G is denoted as *R*. From Fig. 1, we can estimate that the *R* values of 0.89, 1.07, and 1.18 are given by the pristine CNTs, purified CNTs, and Pt/CNTs, respectively. The *R* value rises from 1.22 to 1.33 along with the increasing Co loading from 0.3% to 2.0 wt%. The results indicate that an increased amount of defects is followed by the increase of Co loading amount, and that the Co species strongly interact with the CNTs. In addition, the peaks of the D-band and the G-band slightly shift upwards. This phenomenon can be related to a direct electron charge transfer process between the CNTs and the acceptor moieties such as Co species [40,41]. Nevertheless, the fact that nano-dimension rough metal particles can enhance the Raman response could not be excluded for the changes of *R* value mentioned above [42].

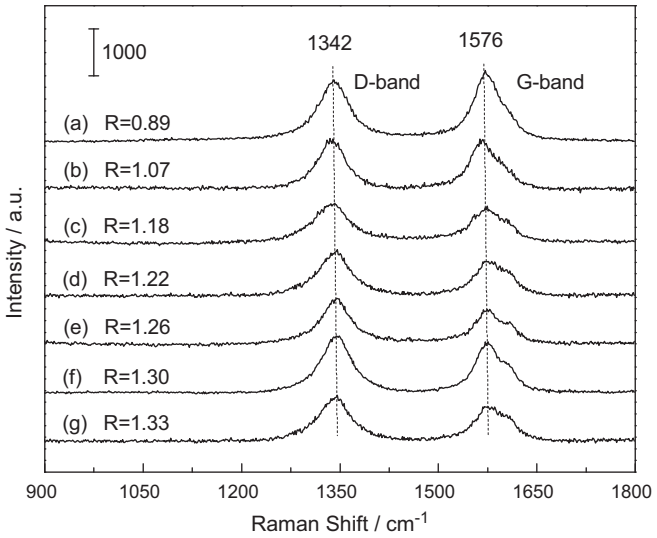

Fig. 1. Raman spectra of CNT, Pt/CNT and Pt-Co/CNTs: (a) pristine CNT; (b) purified CNT; (c) 4.0% Pt/CNT; (d) 4.0% Pt-0.3% Co/CNT; (e) 4.0% Pt-0.7% Co/CNT; (f) 4.0% Pt-1.3% Co/CNT; (g) 4.0% Pt-2.0% Co/CNT.

3.1.3. XRD measurement

The powder XRD patterns for the Pt-Co bimetallic catalysts samples are shown in Fig. 2. All samples show three major peaks at 26.0°, 42.9° and 53.7° corresponding to the graphite planes (0 0 2), (1 0 0) and (0 0 4), respectively. These results indicate the well-graphitized nature of the CNTs after depositing Pt and Co precursors and the subsequently calcined at air atmosphere [43]. The weak diffraction peaks at 2θ of 39.7°, 46.2° and 67.4° are attributed to the cubic platinum metal structure [44]. According to Scherrer's equation, average diameters of Pt nanoparticles can be calculated based on the full width at half maximum of Pt (1 1 1) reflection [43]. However, no characteristic peaks of Pt can be fitted in the XRD patterns of Pt/CNT and Pt-Co/CNTs, indicating that the Pt nanoparticles are less than 4 nm in size and well dispersed on the surfaces of CNTs. Moreover, no peaks corresponding to Co are detected in the Pt-Co/CNTs. Note that the amount of Co loading over the 4.0% Pt-2.0% Co/CNT is twice that of Pt by molar fraction. As a result, most of Co species are possibly either amorphous or highly dispersed on the CNTs, while a small amount of Co species may interact with Pt by forming PtCo alloys during the reduction process.

3.1.4. TEM measurement

The morphologies and structural details of the bimetallic catalysts were examined by TEM. As shown in Fig. 3, the Pt nanoparticles are distributed uniformly on the surfaces of the CNTs, whereas

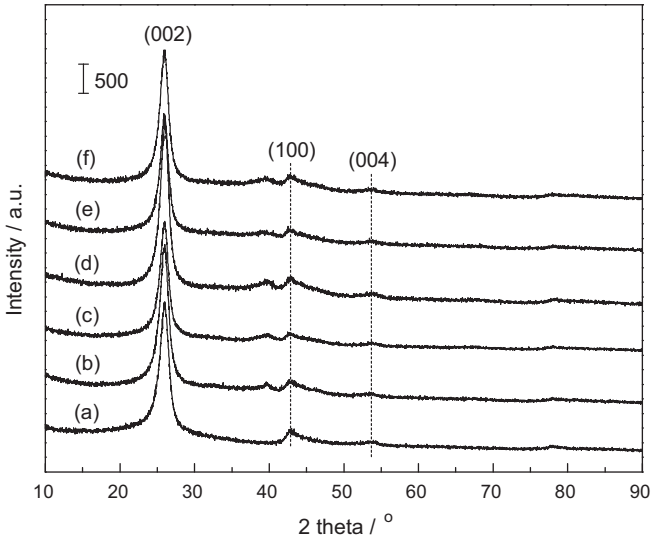

Fig. 2. XRD patterns of CNT, Pt/CNT and Pt-Co/CNTs: (a) purified CNT; (b) 4.0% Pt/CNT; (c) 4.0% Pt-0.3% Co/CNT; (d) 4.0% Pt-0.7% Co/CNT; (e) 4.0% Pt-1.3% Co/CNT; (f) 4.0% Pt-2.0% Co/CNT.

the cobalt-containing particles are hardly detected. This also explains the undistinguished diffraction peaks for Pt and Co phases. The nanoscale elemental mapping and EDX analysis (Fig. 4 and Supplemantary Fig. S1) reveal that most of Co species are distributed on the Pt domain and they can not be clearly distinguished by TEM. These results are in accordance with the results of the XRD pattern and Raman spectroscopy. The corresponding distributions of metal particle sizes are also presented in Fig. 3. All the samples show a sharp distribution of metal particles, centering at 2.4–2.8 nm. Among them, the 4.0% Pt-0.7% Co/CNT exhibits the smallest Pt particles, whereas the other Pt-Co/CNTs and Pt/CNT have a slightly larger mean size. Previous studies have pointed out that the transition metal tends to diffuse into the subsurface of Pt nanoparticles during the reduction process [45]. Thus, the change of average particles size is likely due to the addition of Co species, which may improve the dispersion of Pt nanoparticles in an appropriate amount. In other words, the Co species on the periphery and surface of Pt domain can prevent the Pt nanoparticles from aggregation [46].

3.1.5. XPS measurement

It is worth to note that, the Pt-Co bimetallic catalysts were first reduced and then followed by calcination in air. Before the reaction, no further treatments were carried out. Therefore the electron and oxidization states of Pt and Co entities in the as-prepared Pt-Co/CNTs were characterized by XPS for some typical samples. The XPS results of the Pt 4f and Co 2p for the samples of 4.0% Pt-0.7% Co/CNT, 5.0% Co/CNT, and 4.0% Pt/CNT are shown in Fig. 5. As seen in Fig. 5a, the Co $2p_{3/2}$ peak at BE = 782.1 eV of 4.0% Pt-0.7% Co/CNT is evidently accompanied by strong shake-up satellites; this is characteristic of CoO. The XPS of Co $2p_{3/2}$ differs from that of Co_3O_4 or Co_2O_3 by having a discernable shake-up satellite peak around 4.5–5 eV higher than its main peak and a spin-orbit coupling of approximately 15.5 eV [47], unquestionably confirming the presence of CoO. Another quite small peak for Co $2p_{3/2}$ can be observed at BE = 778.1 eV, which is probably due to the formation of Pt–Co alloys likely Pt_3Co species [20,47,48]. For the XPS of 5.0% Co/CNT, the main peak for Co $2p_{3/2}$ is centered around BE = 780.5 eV, and is without a clear shake-up satellite that can be assigned to the presence of Co_3O_4 or Co_2O_3 species [47]. As shown in Fig. 5b, the XPS spectra show peaks at BE = 71.5 and 72.6 eV assigned to Pt $4f_{7/2}$ level for a Pt^0 and Pt^{2+} species, respectively. After the incorporation of

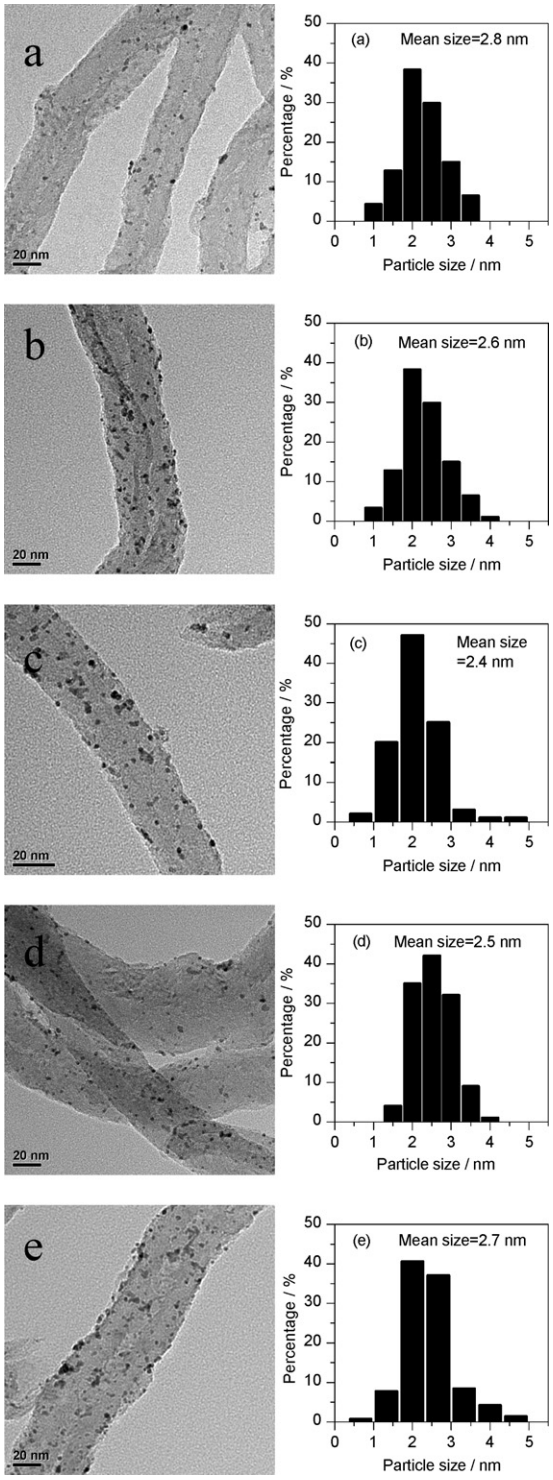

Fig. 3. TEM images and particle size distributions of catalysts with different Co loadings: (a) 4.0% Pt/CNT; (b) 4.0% Pt-0.3% Co/CNT; (c) 4.0% Pt-0.7% Co/CNT; (d) 4.0% Pt-1.3% Co/CNT; (e) 4.0% Pt-2.0% Co/CNT.

Co species into Pt/CNT, the intensity of the XPS peak at BE = 72.6 eV level assigned to Pt^{2+} species increases significantly, whereas the Pt^0 peak intensity remains stable. Therefore, most of Co species exist as CoO that are dispersed and attached on the surfaces of Pt nanoparticles. The difference of chemical state of Co species in the samples of Pt-Co/CNTs and Co/CNT can be ascribed to the existence of metallic Pt, which causes the electron transfer between the Co and Pt species. The delicate modification of the metallic Pt surface

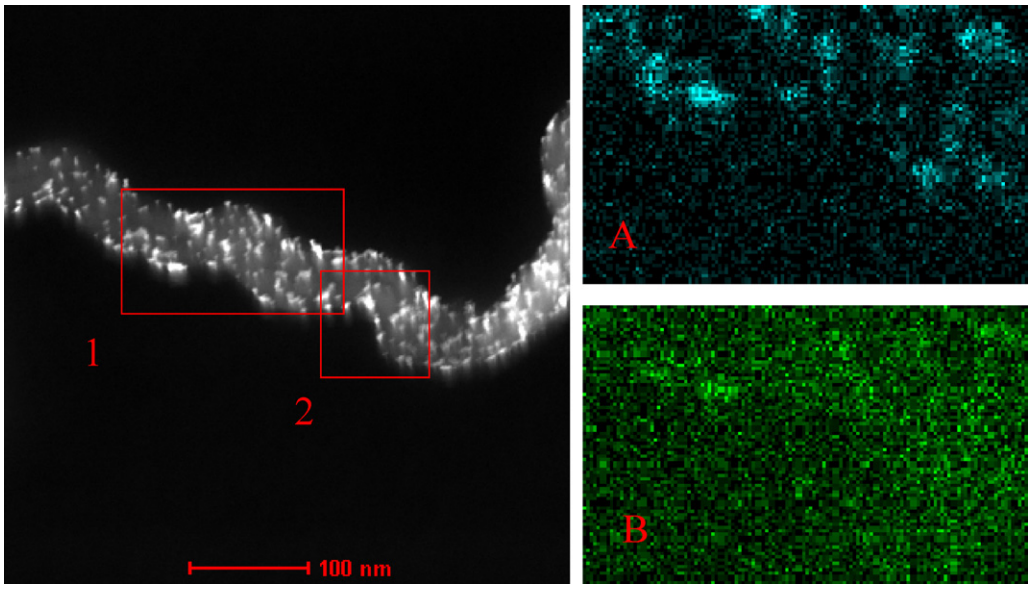

Fig. 4. TEM dark field image of 4% Pt-0.7% Co/CNT catalyst. Elemental EDX maps were taken from area 1. Area 2 was used to correct for any drift of the samples. Map (A) map (B) reflect the measured Pt M intensity and Co L intensity, respectively.

electron density is expected to result in unexpected influences on the surface adsorption behavior and catalytic performance.

3.2. Catalyst activity

3.2.1. Catalytic behavior for CO oxidation reaction

The catalytic performance of Pt-Co/CNTs and Pt/CNT for CO oxidation and CO-PROX reaction are shown in Figs. 6 and 7, respectively. For the CO oxidation reaction, compared to the single component catalyst Pt/CNT, the Pt-Co/CNTs exhibit a much higher activity for the complete conversion of CO. As seen in Fig. 6, the 4.0% Pt/CNT catalyst shows nearly no activity until 393 K, then gives a complete oxidation of CO at 453 K. When 0.3 wt% Co is added, the derived Pt-Co/CNT catalyst shows a CO conversion of 13.2% at 313 K and gives a complete CO conversion at 473 K, which is 20 K lower than the 4.0% Pt/CNT. When the Co loading increases to 0.7 wt%, the activity of the derived Pt-Co/CNT catalyst is further enhanced, and exhibits a CO conversion of 30.3% at 313 K and a complete CO conversion at 393 K. However, the CO conversion activity decreases with the further increase of Co loading from 0.7 to 2.0 wt%. These results indicate that the introduction of Co species into Pt/CNTs can promote the oxidation of CO; however, this promotional effect can be receded by excess Co. We believe that the enhanced catalytic activity would relate to an increased availability of CO-free catalyst surface sites due to the incorporation of Co entities.

3.2.2. Catalytic behavior for CO-PROX reaction in H_2-rich streams

The CO conversion on overall samples is considerably increased by the introduction of H_2 and presents a similar tendency as CO oxidation (Fig. 7). As shown in Fig. 7, the CNT-supported catalyst with 4.0 wt% Pt and 0.7 wt% Co exhibits the best performance, giving a temperature window for complete CO removal ranging from 313 to 433 K. At 313 K, the CO conversion shows a volcano type profile as a function of Co loading (Fig. 7, insert), increasing remarkably from 0% to 100% with the increase of Co loading from zero to 0.7 wt%, and then dropping to about 49% with the further increase of Co loading from 0.7 to 2.0 wt%. The trend of O_2 conversion is similar to CO, but the O_2 selectivity to CO_2 formation declines gradually from 75% to 52%, and then increases up to 98% as a function of Co loading. The same composition of Pt-Co catalysts supported on other carriers and CNT-supported monometallic Co catalyst show lower CO-PROX performance under identical conditions (Table 2). Nevertheless, at higher temperatures (453–473 K), except for the catalysts of 4.0% Pt/CNT and 4.0% Pt-2.0% Co/CNT, the CO conversion and the selectivity of O_2 to CO_2 over the other catalysts decrease gradually, indicating that the Pt species tend to be active with H_2, with high rate in this case. The reverse WGS reaction is not observed over the CNT-supported catalysts, probably owing to the high thermal conductivity of CNTs. Therefore, the promotional effect of H_2 may be attributed to the formation of minor hydrogen-containing oxidizing species, such as the hydroxyl (OH) or carboxyl (COOH) group, which can selectively oxidize CO molecule in a H_2-rich stream [28,49]. At high temperature, however, the generation of excess active hydrogen-containing oxidizing species brings about a drop of O_2 selectivity, leading to a lower CO-PROX performance.

3.2.3. Effect of space velocity

The influence of space velocity on the CO conversion and O_2 selectivity over the catalyst 4.0% Pt-0.7% Co/CNT is displayed in Fig. 8. Under the FW^{-1} of 30,000 mL g^{-1} h^{-1}, 100% CO conversion can be obtained at 313–433 K. The higher the FW^{-1}, the higher the temperature for the requested CO-PROX. Under the FW^{-1} of 60,000 mL g^{-1} h^{-1}, the catalyst affords 100% CO conversion at 333 K; however, FW^{-1} of 90,000 mL g^{-1} h^{-1} can only present a CO conversion of 69.4% at this temperature. Even if the FW^{-1} is adjusted to 120,000 mL g^{-1} h^{-1}, a CO conversion of 100% can still be obtained at 373–433 K. The results indicate that the influence of space velocity on CO removal is significant; however, a complete removal of CO is obtainable at high space velocity by raising the reaction temperature. The O_2 selectivity is kept at 50% when the CO-PROX proceeds under the FW^{-1} investigated, as shown in Fig. 8.

3.2.4. Catalyst stability

To evaluate the stability of the catalyst 4.0% Pt-0.7% Co/CNT, we have performed the CO-PROX with 20% H_2O and 25% CO_2 with a FW^{-1} of 40,000 mL g^{-1} h^{-1} and varying O_2 concentrations. The data of CO conversion and O_2 selectivity were collected after the reaction for 6 h. The O_2 selectivity increases gradually from 50%

Table 2
The comparison of PROX performance over supported Pt-Co and monometallic Co catalysts with different carriers.

Catalyst (Pt = 4.0 wt%, Co = 0.7 wt%)	CO conversion (%)		O_2 selectivity (%)		The lowest temp. (K) for maximum CO conversion
	At 313 K	At 433 K	At 313 K	At 433 K	
5.0% Co/CNT	0	9.2	–	81.6	473 (44.3%)
Pt-Co/CNT	100	100	51.0	50.0	313 (100%)
Pt-Co/AC[a]	75.5	92.8	82.8	45.6	373 (100%)
Pt-Co/GA[b]	18.1	100	92.9	50.0	433 (100%)
Pt-Co/TiO_2	38.6	64.6	89.4	32.9	353 (92.3%)
Pt-Co/SiO_2	76.6	98.8	95.1	48.9	393 (100%)
Pt-Co/γ-Al_2O_3	36.9	100	79.3	50.0	373 (100%)

Reaction conditions: catalyst weight = 0.1 g, feed gas = 1.0% CO + 1.0% O_2 + 50% H_2 balanced with N_2, FW^{-1} = 30,000 mL h^{-1} g-cat^{-1}.
[a] AC: active carbon.
[b] GA: graphite.

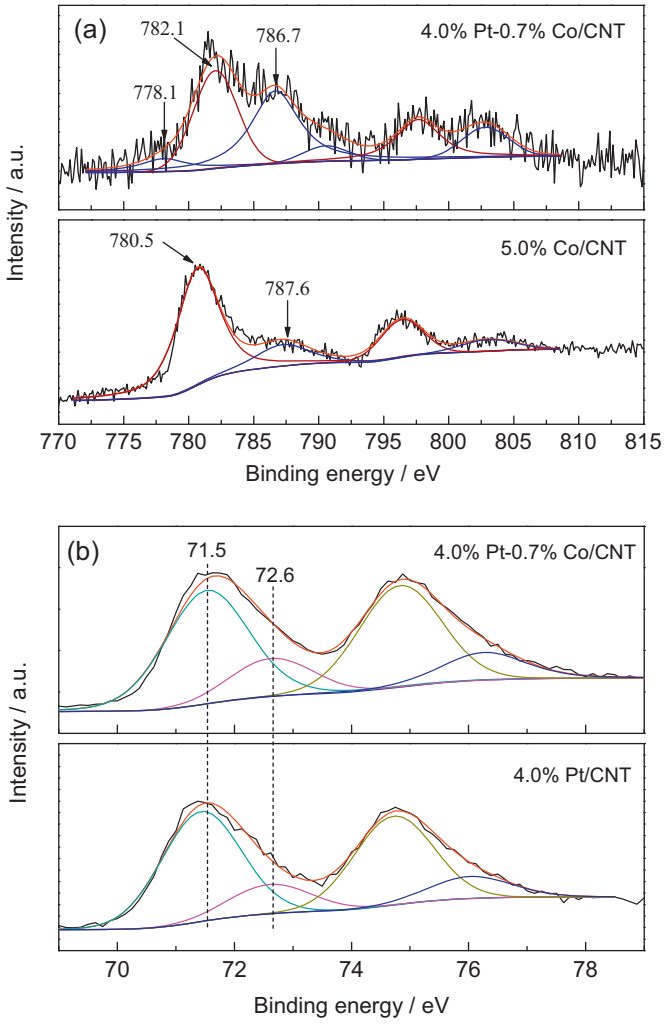

Fig. 5. XPS spectra of (a) Co 2p and (b) Pt 4f for the samples of 4.0% Pt-0.7% Co/CNT, 5.0% Co/CNT, and 4.0% Pt/CNT, respectively.

to 95.5% when the O_2 concentration is decreased from 1.0% to 0.5% as depicted in Fig. 9. Meanwhile, the CO conversion maintains 100% until the O_2 concentration reduces to 0.7%; it then decreases markedly with the further decrease of O_2 concentration. Among O_2 concentrations tested, the catalyst under the O_2 concentration of 0.7% exhibits the best CO conversion and highest O_2 selectivity.

Next, the CO-PROX with 20% H_2O and 25% CO_2 over the catalyst 4.0% Pt-0.7% Co/CNT was conducted at 353 K as a function of time on stream. As illustrated in Fig. 10, 100% CO conversion and 62.7% O_2 selectivity were maintained for 50 h under an O_2 concentration of 0.8% and a FW^{-1} of 40,000 mL g^{-1} h^{-1}. Subsequently, 100% CO conversion and 71.4% O_2 selectivity were maintained for another additional 50 h under an O_2 concentration of 0.7% and the FW^{-1} of 40,000 mL g^{-1} h^{-1}. The structure of CNTs is kept intact during the long-term CO-PROX reaction under present conditions, as evidenced by TEM measurements (not shown). The results demonstrate that the catalyst 4.0% Pt-0.7% Co/CNT can perform high CO-PROX activity with excellent stability and tolerance to CO_2 and H_2O vapor, showing very promising results for PEMFC application.

3.2.5. O_2–H_2 titration

The surface Pt states of several catalysts under different conditions were determined by means of O_2–H_2 titration and XPS measurement. As expected, the catalyst samples exposed to air have hardly O_2 uptake (Supplemantary Table 1S). The metal dispersions of CNT supported catalysts with similar particle size (see Fig. 3) reduced with H_2 at 523 K decrease with the increase of Co loading (Table 3). The metal dispersion data have been confirmed by H_2 titration using stoichiometry H/Pt = 3 (Table 3). In all cases, the dispersion calculated by H_2 titration is slightly higher than that given by O_2 titration, but the data by these two methods are in

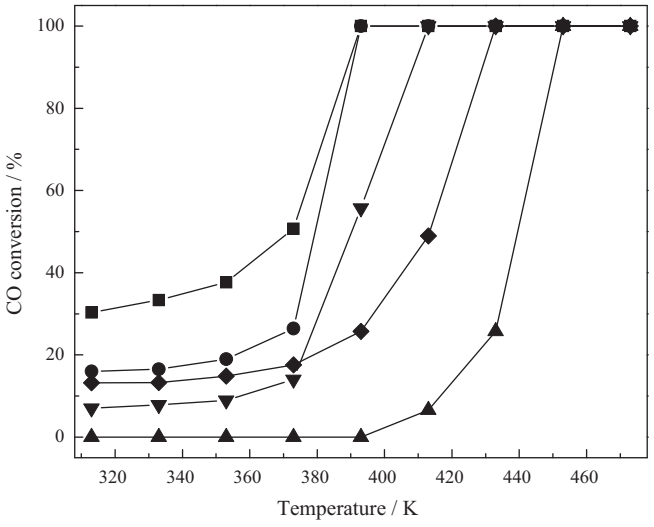

Fig. 6. The performance of CO oxidation over Pt-Co/CNTs with different Co loadings. (▲) 4.0%Pt/CNT; (♦) 4.0% Pt-0.3% Co/CNT; (■) 4.0% Pt-0.7% Co/CNT; (●) 4.0% Pt-1.3% Co/CNT; (▼) 4.0% Pt-2.0% Co/CNT. Feed gas: 1% CO and 1% O_2 balanced with N_2 using FW^{-1} = 30,000 mL g^{-1} h^{-1}.

Table 3
Results of O_2–H_2 titration and TOF over several supported Pt and Pt-Co catalysts.

Sample	Metal dispersion (%)[a]				TOF at 313 K $\times 10^{-3}$ (s^{-1})
	By TEM[a]	$O/Pt_{523\text{-red}}$[b]	$H/Pt_{313\text{-oxid}}$[c]	$O/Pt_{313\text{-react}}$[d]	
4.0% Pt/CNT	40.0	39.9	40.3	27.0	0.8
4.0% Pt-0.7% Co/CNT	47.0	28.6	30.0	26.0	66.0
4.0% Pt-2.0% Co/CNT	41.0	20.7	24.2	15.0	57.0
4.0% Pt-0.7% Co/γ-Al_2O_3	61.0	58.0	60.0	55.0	12.0

[a] All the Pt particles were regarded as the spheres. Thus, the Pt dispersion, D, was calculated as $D = (6\upsilon_m/a_m d) \times 100\%$, according to literature, where, D is the Pt dispersion; υ_m is the volume of a Pt atom, $\upsilon_m = (M/\rho N_o)$, M is the molecular weight of Pt, ρ is the density of Pt, N_o is Avogadro constant; a_m is the area of a Pt atom on the surface, $a_m = 1/(1.25 \times 10^{19})$; and d is the Pt particle diameter determined by TEM. Therefore, $D = 1.13/d$.
[b] $Pt_{533\text{-red}}$: metallic Pt in the sample reduced by H_2 at 523 K.
[c] $Pt_{313\text{-oxid}}$: metallic Pt in the sample reacted with O_2 at 313 K.
[d] $Pt_{313\text{-react}}$: metallic Pt in the sample reacted with feed gas of 1% CO, 1% O_2, and 50% H_2 balanced with N_2 at 313 K.

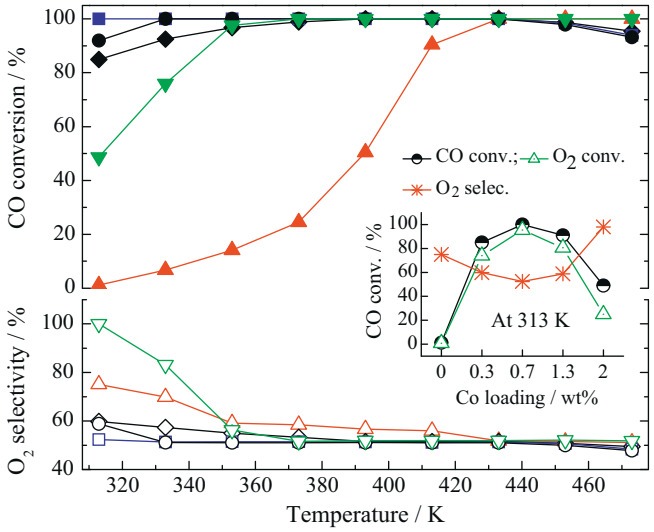

Fig. 7. The performance of CO-PROX over Pt-Co/CNTs with different Co loadings. Filled symbols: CO conversion; open symbols: O_2 selectivity (▲ and △) 4.0% Pt/CNT; (◆ and ◇) 4.0% Pt-0.3% Co/CNT; (■ and □) 4.0% Pt-0.7% Co/CNT; (● and ○) 4.0% Pt-1.3%Co/CNT; (▼ and ▽) 4.0% Pt-2.0% Co/CNT. Insert: Conversions of CO and O_2, and O_2 selectivity as a function of Co loading at 313 K. Feed gas: 1% CO, 1% O_2, 50% H_2 balanced with N_2 using FW^{-1} = 30,000 mL g^{-1} h^{-1}.

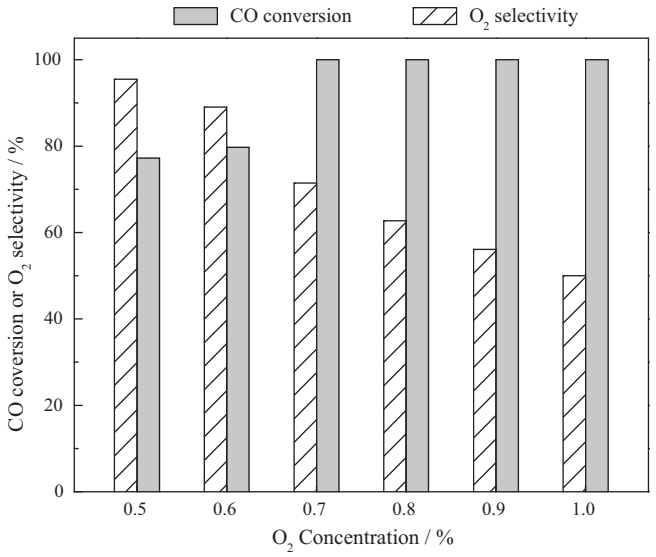

Fig. 9. Dependence of O_2 concentration on the performance of 4.0% Pt-0.7% Co/CNT at 353 K. Feed gas: 1% CO, 0.5–1.0% O_2, 25% CO_2, 20% H_2O, and 50% H_2 balanced with N_2 using FW^{-1} = 40,000 mL g^{-1} h^{-1}.

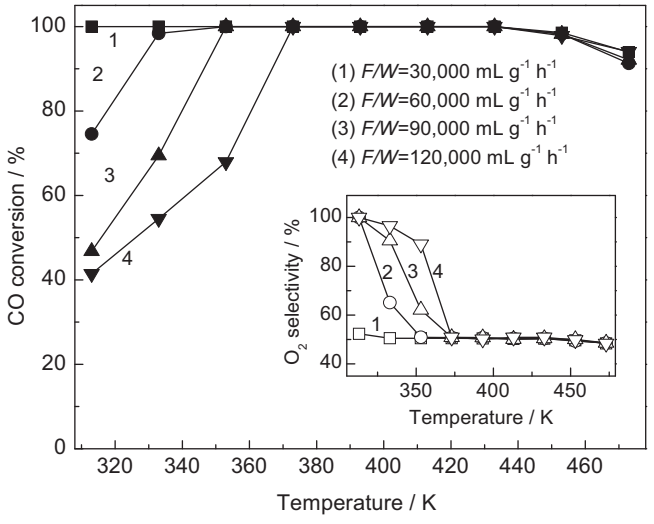

Fig. 8. Effect of FW^{-1} on CO conversion (filled symbols) and O_2 selectivity (insert, open symbols) over the 4.0% Pt-0.7% Co/CNT catalyst in PROX reaction. Feed gas: 1% CO, 1% O_2, and 50% H_2 balanced with N_2.

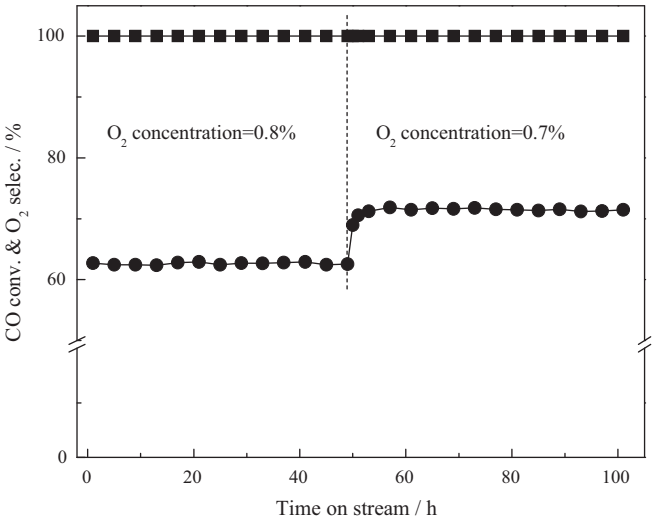

Fig. 10. CO-PROX of 4.0%Pt-0.7%Co/CNT at 353 K as a function of time on stream. (■): CO conversion; (●): O_2 selectivity. Feed gas: 1% CO, 0.7–0.8% O_2, 25% CO_2, 20% H_2O, and 50% H_2 balanced with N_2 using FW^{-1} = 40,000 mL g^{-1} h^{-1}.

good agreement and show a similar decreasing tendency with the increasing of cobalt content. The results indicate that some portion of CoO species may block the surface of Pt nanoparticles. Another evidence for the blockage of the CoO species is gained by the CO-TPD profiles of the Pt-Co/CNTs (Supplemantary Fig. S2). The results reveal that the incorporation of Co species depresses or inhibits the CO absorption on the catalyst surfaces. One probability is the electron transfer between the Pt and Co species, and another is due to the coverage of CoO species, both resulting in weak CO-adsorption on the Pt surfaces.

After the oxidized catalysts are exposed to the reaction feed gas containing 1% CO + 1% O_2 + 50% H_2 balanced with N_2 at 313 K for 3×10 min, they show metal dispersions lower than the corresponding samples by H_2-reduction at 523 K, but the portion of metallic Pt in the catalysts with cobalt species is higher than that in the Pt/CNT one (Table 3). When the oxidized catalysts are exposed to the reaction feed gas at 353 K for 3×10 min, the ones with cobalt species give metal dispersions close to the corresponding samples by H_2-reduction at 523 K, while the Pt/CNT without cobalt species presents a dispersion appreciably lower than the corresponding sample by H_2-reduction at 523 K (Supplemantary Table 1S). These indications suggest that the surface PtO_x species in the CNT-supported Pt-based catalysts can be partially or entirely reduced in a stream containing 1% CO + 1% O_2 + 50% H_2 balanced with N_2, but the metallic Pt concentration after exposure to the feed gas is related to the Co loading and temperature. Thereby, the results of O_2–H_2 titration imply that the bimetallic PtCo/CNT catalyst is more active for the activation of oxygen molecule at lower temperatures in comparison with Pt/CNT.

The exact oxidation states of the metal species on the 4%Pt-0.7%Co/CNT catalyst after reduction and oxidation have been examined by XPS. As can be seen in Supplemantary Fig. S3, the binding energy of Pt in the 4f binding region can be deconvoluted and fitted with doublet peaks: one at BE = 71.5 eV can be attributed to metallic Pt and another at BE = 72.6 eV can be assigned to Pt^{2+} species. The area ratio of metallic Pt and oxidized Pt appreciably increases after the O_2 titration. This phenomenon is ascribed to the formation of Pt–O species on the catalyst surface after O_2 titration. On the other hand, the Co 2p spectra in the 4%Pt-0.7%Co/CNT catalyst after the reduction and oxidation are evidently accompanied by strong shake-up satellites of characteristic CoO species, showing no obviously changes in the oxidation state. Meanwhile, the small peak for Co $2p_{3/2}$ at BE = 778.1 eV assignable to Pt_3Co alloy species is sustained after the O_2 titration, suggesting that the phase separation of this Pt–Co alloy phase could be excluded under present conditions. Therefore, we conclude that the oxidation states of cobalt species without changes significantly before and after the O_2 titration may eventually be due to strong interactions between Pt and Co species and relatively mild working conditions.

The TOF at 313 K over the samples in Table 3 increases markedly with the incorporation of small amount of Co to Pt/CNT catalyst and the highest TOF is obtained with a Pt-Co/CNT catalyst containing Co of 0.7 wt%. Further increase of Co loading causes a drop of TOF value. These results are in good accord with O_2 conversion as shown in Fig. 7 (insert). When the same composition is supported on γ-Al_2O_3, the catalyst thus obtained exhibits very low TOF under identical conditions.

It is known that the adsorption of O_2 on the freshly reduced supported Pt catalyst can lead to the formation of the Pt–O surface and can also undergo the transformation of Pt–O to Pt–CO by removing the O_{ads} as CO_2 with the introduction of CO at ambient temperature [50]. The CO molecule strongly and almost exclusively adsorbed onto Pt catalysts and the dilute O_2 concentration in the feed gas can inevitably result in the unavailability of active oxygen, which is essential for the CO-PROX at lower-temperatures. Therefore, it is reasonable to speculate that the adsorption and activation of molecular oxygen could primarily occur on CoO. A proper amount of CoO on the periphery of Pt nanoparticles is crucial for achieving superior CO-PROX performance at lower temperatures. In other word, the well-matching activations of oxygen by CoO and of CO by Pt could render a catalyst with high CO-PROX performance. Nonetheless, the perfect alignment of lattices along the CNT axis and the curvature of graphite-like planes can bring about several novel properties to CNT, such as defect sites and functional groups on the surface, electrical conductivity, and chemical stability compared to traditional carriers [51,52]. These properties can also be favorable for the electron transfer rates of reaction and the desorption of products.

4. Conclusion

The Pt-Co/CNTs bimetallic catalysts prepared by the wet co-impregnation method followed by liquid phase reduction and calcination are able to efficiently remove CO in H_2-rich stream by preferential oxidation. The optimized catalyst with 0.7% Co and 4.0% Pt is able to completely remove the CO at temperatures ranging from 313 to 433 K, where the O_2 selectivity to CO_2 formation is kept at approximately 50%. The O_2 selectivity can be enhanced to above 70% while keeping CO conversion at 100% when the molar ratio of CO/O_2 is adjusted to 1/0.7. The catalyst 4.0% Pt-0.7% Co/CNT can maintain 100% CO conversion and above 50% selectivity of O_2 in a feed gas containing 25% CO_2 and 20% H_2O vapor at 353 K for longer than 100 h. These results cannot be obtained with same composition of Pt and Co supported on other carriers. The XRD and TEM results indicate that the Pt nanoparticles with mean size of 2–3 nm are uniformly dispersed on the catalyst surfaces, whereas the particle sizes of Co species are below detectable limits. The results of X-ray photoelectron spectroscopy and nanoscale elemental mapping indicate that most of Co species are in the form of CoO, presenting on the periphery and surface of Pt domain. O_2 titration and kinetic studies show evidence that the CoO on the periphery of Pt nanoparticles is involved in the CO-PROX reaction, acting as an oxygen supply. The proper atomic ratio of Pt/Co along with the choice of support is key issues for a Pt-Co/CNT bimetallic catalyst with high CO-PROX performance at lower temperatures. We conclude that, in addition to the effect of support, the synergistic interaction between Pt metal surface and CoO are largely responsible for the high CO-PROX performance of Pt-Co/CNTs.

Acknowledgement

We gratefully acknowledge the financial support from the National Basic Research Program of China (no. 2011CBA00508), the Natural Science Foundation of China (nos. 20923004 and 21173175) and the Program for Changjiang Scholars and Innovative Research Team in University (no. IRT1036).

Appendix A. Supplementary data

Supplementary data associated with this article can be found, in the online version, at doi:10.1016/j.jpowsour.2011.11.044.

References

[1] B.C.H. Steele, A. Heinzel, Nature 414 (2001) 345–352.
[2] D.L. Trimm, Appl. Catal. A: Gen. 296 (2005) 1–11.
[3] H.Wang, H.Q. Zhu, Z.F. Qin, F.X. Liang, G.F. Wang, J.G. Wang, J. Catal. 264 (2009) 154–162.
[4] O. Pozdnyakova-Tellinger, D.Teschner, J. Kröhnert, F.C. Jentoft, A. Knop-Gericke, R. Schlögl, A. Wootsch, J. Phys. Chem. C 111 (2007) 5426–5431.
[5] E. Cho, J. Ko, H.Y. Ha, S. Hong, K. Lee, T. Lim, I. Oh, J. Electrochem. Soc. 15012 (2003) A1667–A1670.
[6] S. He, M.M. Mench, J. Electrochem. Soc. 1539 (2006) A1724–A1731.
[7] M. Echigo, T. Tabata, Catal. Today 90 (2004) 269–275.

[8] M. Echigo, N. Shinke, S. Takami, S. Higashiguchi, K. Hirai, T. Tabata, Catal. Today 84 (2003) 209–215.
[9] S. Kawatsu, J. Power Sources 71 (1998) 150–155.
[10] M.J. Kahlich, H.A. Gasteiger, R.J. Behm, J. Catal. 171 (1997) 93–105.
[11] F. Arena, P.Famulari, G. Trunfio, G. Bonura, F. Frusteri, L. Spadaro, Appl. Catal. B: Environ. 66 (2006) 81–91.
[12] S.H. Oh, R.M. Sinkevitch, J. Catal. 142 (1993) 254–262.
[13] M. Kuriyama, H. Tanaka, S. Ito, T. Kubota, T. Miyao, S. Naito, K. Tomishige, K. Kunimori, J. Catal. 252 (2007) 39–48.
[14] H. Wakita, K. Ukai, T. Takeguchi, W. Ueda, J. Phys. Chem. C 111 (2007) 2205–2211.
[15] Y.F. Ham, M.Kinne, R.J. Behm, Appl. Catal. B: Environ. 52 (2004) 123–134.
[16] S.J. Huang, K.J. Hara, A. Fukuoka, Energy Environ. Sci. 2 (2009) 1060–1068.
[17] J. Choi, C.B. Shin, D.J. Suh, Catal. Commun. 9 (2008) 880–885.
[18] A. Sirijaruphan, J.G Goodwin Jr., R.W. Rice, J. Catal. 224 (2004) 304–313.
[19] E.Y. Ko, E.D. Park, K.W. Seo, H.C. Lee, D. Lee, S. Kim, Catal. Lett. 110 (2006) 275–279.
[20] K. Takayuki, T. Asako, J. Catal. 258 (2008) 306–314.
[21] F. Wang, G.X. Lu, J. Power Sources 181 (2008) 120–126.
[22] H. Tanaka, M. Kuriyama, Y. Ishida, S.-I. Ito, K. Tomishige, K. Kunimori, Appl. Catal. A: Gen. 343 (2008) 117–124.
[23] W.S. Epling, P.K. Cheekatamarla, A.M. Lane, J. Chem. Eng. 93 (2003) 61–68.
[24] D.J. Suh, C. Kwak, J.-H. Kim, S.M. Kwon, T.-J. Park, J. Power Sources 142 (2005) 70–74.
[25] E.-Y. Ko, E.D. Park, H.C. Lee, D. Lee, S. Kim, Angew. Chem. Int. Ed. 46 (2007) 734–737.
[26] P. Landon, J. Ferguson, B.E. Solsona, T. Garcia, A.F. Carley, A.A. Herzing, C.J. Kiely, S.E. Golunski, G.J. Hutchings, Chem. Commun (2005) 3385–3387.
[27] G. Avgouropoulos, T. Ioannides, C. Papadopoulou, J. Batista, S. Hocevar, H. Matralis, Catal. Today 75 (2002) 157–167.
[28] K. Tanaka, M. Shou, H.B. Zhang, Y.Z. Yuan, T. Hagiwara, A. Fukuoka, Catal. Lett. 126 (2008) 89–95.
[29] H.W. Yang, G.Q. Yi, H.Q. Lin, K. Tanaka, Y.Z. Yuan, Chin. J. Catal. 30 (2009) 780–785.
[30] K. Tanaka, M. Shou, Y.Z. Yuan, J. Phys. Chem. C 114 (2010) 16917–16923.
[31] H.W. Yang, C. Wang, B.D. Li, H.Q. Lin, K. Tanaka, Y.Z. Yuan, Appl. Catal. A: Gen. 402 (2011) 168–175.
[32] P. Chen, H.B. Zhang, G.D. Lin, Q. Hong, K.R. Tsai, Carbon 35 (1997) 1495–1501.
[33] J.R. Anerson, Structure of Metallic Catalysts, Academic Press, New York, 1975, p. 296.
[34] N. Mahata1, V. Vishwanathan, J. Catal. 196 (2000) 262–270.
[35] G.Q. Yi, Z.N. Xu, G.C. Guo, K. Tanaka, Y.Z. Yuan, Chem. Phys. Lett. 479 (2009) 128–132.
[36] A. Kongkanand, K. Vinodgopal, S. Kuwabata, P.V. Kamat, J. Phys. Chem. B 110 (2006) 16185–16188.
[37] U.M. Graham, A. Dozier, R.A. Khatri, M.C. Bahome, L.L. Jewell, S.D. Mhlanga, N.J. Coville, B.H. Davis, Catal. Lett. 129 (2009) 39–45.
[38] E.F. Antunes, A.O. Lobo, E.J. Corat, V.J. Trava-Airoldi, Carbon 45 (2007) 913–921.
[39] T. Belin, F. Epron, Mater. Sci. Eng. 119 (2005) 105–118.
[40] A.M. Rao, S. Bandow, E. Ritchter, P.C. Eklund, Thin Solid Films 331 (1998) 141–147.
[41] A.G. Souza Filho, V. Meunier, M. Terrones, B.G. Sumpter, E.B. Barros, F. Villalpando-Paez, J.M. Filho, Y.A. Kim, H. Muramatsu, T. Hayashi, M. Endo, M.S. Dresselhaus, Nano Lett. 7 (2007) 2383–2388.
[42] A. Campion, P. Kambhampati, Chem. Soc. Rev. 27 (1998) 241–250.
[43] Z.T. Liu, C.X. Wang, Z.W. Liu, J. Lu, Appl. Catal. A: Gen. 344 (2008) 114–123.
[44] S. Chytil, W.R. Glomm, E.A. Blekkan, Catal. Today 147 (2009) 217–223.
[45] R.T. Mu, Q. Fu, H. Xu, H. Zhang, Y.Y. Huang, Z.##S. Jiang, Zhang D.L. Tan, X.H. Bao, J. Am. Chem. Soc. 133 (2011) 1978–1986.
[46] Z. Guo, Y.T. Chen, L.S. Li, X.M. Wang, G.L. Haller, Y.H. Yang, J. Catal. 276 (2010) 314–326.
[47] Z. Zsoldos, L. Guczi, J. Phys. Chem. 96 (1992) 9393–9400.
[48] U. Bardi, B.C. Beard, P.N. Ross, J. Catal. 124 (1990) 22–29.
[49] K. Tanaka, M. Shou, H. He, X.Y. Shi, X.L. Zhang, J. Phys. Chem. C 113 (2009) 12427–12433.
[50] A. Bourance, D. Bianchi, J. Catal. 202 (2001) 34–44.
[51] K.P. Gong, S. Chakrabarti, L.M. Dai, Angew. Chem. Int. Ed. 47 (2008) 5446–5450.
[52] J. Zhang, X. Liu, R. Blume, A.H. Zhang, R. Schlögl, D.S. Su, Science 322 (2008) 73–77.